Segmented tomographic evaluation of structural degradation of carbon support in proton exchange membrane fuel cells

Jung A. Hong [a,1], Min-Hyoung Jung [a,1], Sung Yong Cho [b,1], Eun-Byeol Park [a], Daehee Yang [a], Young-Hoon Kim [a], Sang-Hyeok Yang [a], Woo-Sung Jang [a], Jae Hyuck Jang [c], Hyo June Lee [b], Sungchul Lee [b,*], Hu Young Jeong [d,*], Young-Min Kim [a,*]

[a] Department of Energy Science, Sungkyunkwan University (SKKU), Suwon 16419, Republic of Korea
[b] Fuel Cell Core Parts Development Cell, Hyundai Mobis Co. Ltd., Uiwang 16082, Republic of Korea
[c] Electron Microscopy & Spectroscopy Team, Korea Basic Science Institute (KBSI), Daejeon 34133, Republic of Korea
[d] Graduate School of Semiconductor Materials and Devices Engineering, Ulsan National Institute of Science and Technology (UNIST), Ulsan 44919, Republic of Korea

ARTICLE INFO

ABSTRACT

The variation of the three-dimensional (3D) structure of the membrane electrode of a fuel cell during proton exchange cycling involves the corrosion/compaction of the carbon support. The increasing degradation of the carbon structure continuously reduces the electrocatalytic performance of proton exchange membrane fuel cells (PEM-FCs). This phenomenon can be explained by performing 3D tomographic analysis at the nanoscale. However, conventional tomographic approaches which present limited experimental feasibility, cannot perform such evaluation and have not provided sufficient structural information with statistical significance thus far. Therefore, a reliable methodology is required for the 3D geometrical evaluation of the carbon structure. Here, we propose a segmented tomographic approach which employs pore network analysis that enables the visualization of the geometrical parameters corresponding to the porous carbon structure at a high resolution. This approach can be utilized to evaluate the 3D structural degradation of the porous carbon structure after cycling in terms of local surface area, pore size distribution, and their 3D networking. These geometrical parameters of the carbon body were demonstrated to be substantially reduced owing to the cycling-induced degradation. This information enables a deeper understanding of the degradation phenomenon of carbon supports and can contribute to the development of stable PEM-FC electrodes.

© 2022 Science Press and Dalian Institute of Chemical Physics, Chinese Academy of Sciences. Published by ELSEVIER B.V. and Science Press. This is an open access article under the CC BY-NC-ND license (http://creativecommons.org/licenses/by-nc-nd/4.0/).

1. Introduction

Extensive research has been performed to achieve the efficiency and durability requirements for heavy-duty vehicle applications owing to the development of cost-effective and durable proton exchange membrane fuel cells (PEM-FCs) in recent years [1–4]. The research has been primarily focused on the design of membrane electrode assemblies (MEAs), which are considered the most promising electrochemical-generating devices, due to their high energy efficiency and high power density; they can be implemented in various applications including chemical sensors, electrochemical devices, batteries, supercapacitors, and power generation [5–9]. A porous carbon body is used as the essential component in both the electrodes of a typical MEA to support the catalyst particles and ion conducting polymer layer [10]. During the normal operation of PEM-FCs, their electrochemical performance gradually decreases due to the deterioration of the electrochemical surface area (ECSA) of the catalyst, reducing their durability for practical applications. The deterioration of the ECSA is primarily attributed to the gradual increase of the electrical isolation of the catalyst particles, which may be caused by the chemical corrosion of the carbon support, accompanied by the damage of the ion conducting polymer surface layer [10–12]. Therefore, carbon corrosion is considered a key symptom which arises from the degradation of the PEM-FC during operation [13]. Furthermore, the structural compaction of the porous carbon support that occurs during the FC operation can

reduce the mass transport properties in the electrodes owing to the reduction of the pore connectivity within the carbon body [14]. The structural stability of the electrodes significantly affects the resulting FC performance; therefore, a reliable and accurate analysis of the change in the carbon structure during the FC operation is crucial to achieving a better understanding of the degradation phenomenon of the PEM-FCs, which further facilitates the development of effective engineering strategies for durable PEMs [15].

Three-dimensional (3D) electron tomography based on focused ion beam-equipped scanning electron microscopy (FIB-SEM) serial section technique [16] has been implemented to address the structural degradation of the porous carbon support [17]. A series of 2D SEM images of an object is continuously recorded during the FIB serial sectioning and then used in the 3D volume reconstruction of the object following digital processing in the resolving scale which ranges from ∼10–1000 nm [17–19]. The artificial volume reconstruction technique is considered an essential tool for the visualization and analysis of the 3D nature of porous materials with nanometric structural changes since it presents a much higher spatial resolution than X-ray computed tomography [20]. However, the significance of statistical interpretation on tomographic volumes has been overlooked due to the requirement of a heavy load of human input during the multiple acquisition and processing of the tomography dataset. The resulting information is insufficient and presents considerable challenges in the correlation of the changes of the geometrical structure parameters to the FC performance during operation, thus limiting a wider application of this approach. For example, microporosity has been measured as a representative geometrical parameter of a reconstructed volume of the porous carbon support before and after the degradation cycling [21]. However, the difference between the measured microporosities and their connectivity is typically negligible in determining the effect of the carbon corrosion on the structural deterioration as demonstrated in this study. The simple measurement of global porosity of the carbon body cannot highlight detailed structural changes after degradation cycling, as the structural change caused by carbon corrosion can be resolved at the nanometric scale. Therefore, the measurement process must be focused on evaluating the changes in the localized structure parameters such as local surface area, pore sizes, and pore-to-pore networking within the porous carbon body.

Consequently, we have developed an advanced FIB-SEM tomography process to visualize the localized structure parameters at the nanoscale, which is achieved by performing the digital segmentation of a large tomographic volume along with the pore network analysis for the segmented volumes. Based on this approach, we demonstrate that the reduced electrochemical performance of the PEM-FC is closely correlated to the degradation of the carbon support under the 100 nm scale regime. The surface area of the carbon support was considerably reduced after FC cycling, whereas the change in the overall porosity was marginal. Our segmented tomography results demonstrate that small pores below 100 nm were preferentially annihilated during degradation cycling, while the larger pores ($\geq$200 nm) were almost unaffected. Furthermore, the 3D connectivity of the pores within the carbon body was notably decreased, presumably causing the gradual constriction of mass transport inside the electrode during FC operation. The proposed method unequivocally provides crucial information, enabling a better understanding of the microscopic origin of the carbon corrosion behavior, which has not been achieved by conventional approaches.

2. Experimental

2.1. PEM synthesis and electrochemical measurements

The Pt/Co alloy catalyst (45.0 wt% Pt/Co-carbon, TEC36F52, Tanaka Kikinzoku Kogyo K.K., TKK), which is commercially available, was used as an electrocatalyst for electrodes in the construction of PEM-based fuel cell. The Pt/Co alloy catalysts improve the oxygen reduction reaction activity while using low Pt content, whereas they show relatively inferior durability during high current density fuel cell operations due to mass-transport losses [1,22]. The loading of Pt/Co was set to be 0.3 mg/cm^2. The electrocatalyst ink was then prepared using a blend of Pt/Co, 50% ultra-pure water, 50% 1-propanol, and a 1100 EW solubilized ionomer (Nafion ionomer) which was used for the electrodes at an ionomer/carbon weight ratio (IC ratio) of 0.8. The electrocatalyst electrode layers were coated onto both sides of a patterned Nafion membrane using a spray printing method. The fuel cell structure was then manufactured using a conventional hot-pressing-assisted sandwich process [23]. Fig. 1(a) depicts a typical MEA-based fuel cell structure. To examine the electrochemical stability of the synthesized MEA sample, voltage cycling (VC) testing was performed with the condition of rectangular sweep cycle between 0.6–0.95 V and the duration time of each voltage was 3 s. The ambience condition for the VC operation was 50% relative humidity of H$_2$ (1.5 stoichiometry anode) and air (2.0 stoichiometry cathode) at 65 °C. The MEA sample were subjected to 5000 cycles and the performance degradation between the pristine and degraded samples was accessed by measuring the *I-V* polarization curves that were conducted in a galvanostatic mode under the respective 50% relative humidity of H$_2$ (stoichiometry of 1.5) and air (stoichiometry of 2.0) at 65 °C under atmospheric pressure [24].

2.2. Cross-section sampling and characterizations

Several approaches were employed to prepare the cross-sectional structures and thin lamellas of the MEA samples for scanning electron microscopy (SEM, JSM5600F, JEOL) and scanning transmission electron microscopy (STEM, ARM200CF and Mono-ARM200, JEOL). They include: freeze-fracture processing, ultramicrotomy (EM UC7, Leica), and focused ion beam (FIB, Helios Nano-Lab 450, FEI) slicing technique. The thin cryo-sections cut by the ultramicrotome do not suffer from ion-beam damage despite its relatively large sectioning thickness. Therefore, the sectioned MEA lamella was used as the reference sample to set up the slicing condition of the Ga ion beam FIB to produce a nearly damage-free TEM thin sample and serial sectioning for tomography reconstruction. The annula dark field (ADF) and annular bright field (ABF) imaging modes of an aberration-corrected STEM instrument operating at 200 kV with the probe angle of ∼23 mrad were employed to analyze the cross-sectional structures of the MEA samples. The detector angle ranges for the ADF and ABF imaging modes were set to 45–175 and 12–24 mrad, respectively. Energy dispersive X-ray spectroscopy (EDX) elemental mapping of the MEA lamella samples was performed in the ADF STEM imaging mode using an EDX spectrometer (JED-2300 T, JEOL) with a dual-type silicon drift detector that had a large effective solid angle of ∼1.2 sr.

2.3. Serial section electron tomography

The FIB-SEM-based serial section imaging method was employed to obtain a series of 2D SEM images during continuous FIB sectioning, which is consecutively used to construct a 3D vol-
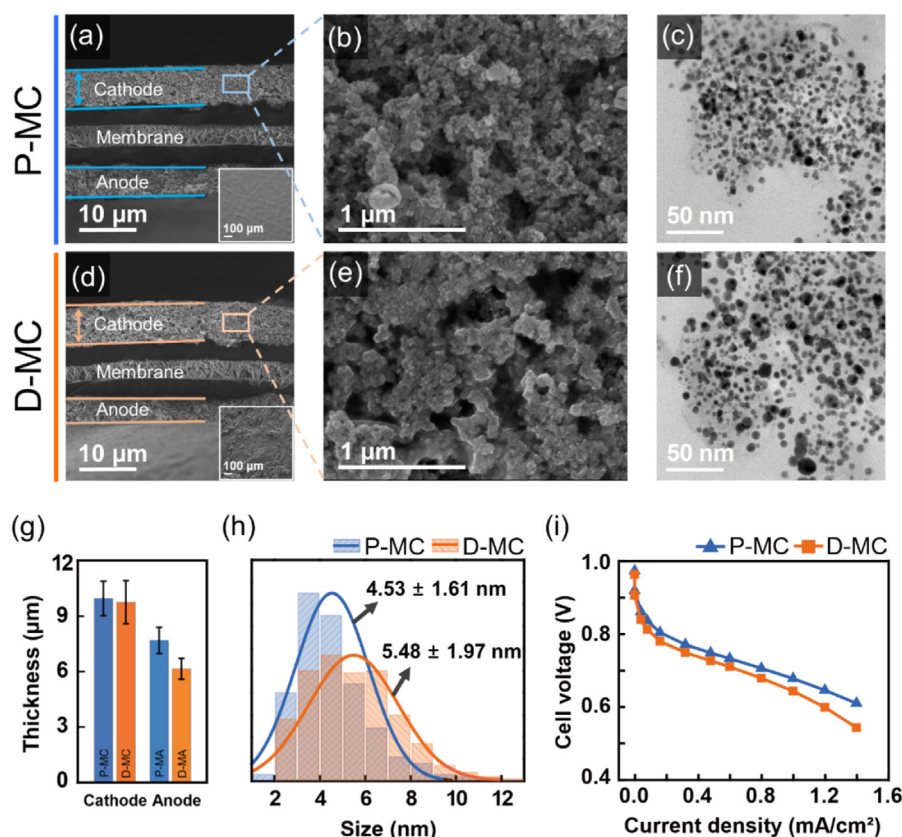
Fig. 1. Cross-sectional structure analysis of PEM-FC before and after 5000 proton exchange cycles (P-MC and D-MC, respectively). SEM images depicting the (a) overall cross-sectional structure of the P-MC sample and (b) porous structure of cathode layer before cycling. Insets in (a and b) depict the surface morphologies before and after the degradation cycling. (c) High-magnification ABF STEM image of the cathode layer prepared by ultramicrotome sectioning. (d–f) Equivalent data array for the D-MC sample. (g) Measurements of electrode thickness before and after the cycling. (h) Histograms showing the size distribution of Pt/Co catalyst particles before and after the cycling. (i) I-V characteristics of the PEM samples before and after 5000 cycles.

ume for a tested sample by using an image-wise digital alignment. The attainable spatial resolution is generally superior to that obtained using X-ray computed tomography, which is essential for the 3D analysis of nanometric structure variations. In this tomography setup, the tomographic resolution, defined as the voxel dimension, was 6.4 nm × 6.4 nm × 15 nm. The FIB-SEM instrument (FIB, Helios NanoLab 450, FEI) was used to obtain serial section images of the MEA samples before and after proton exchange cycling for electron tomography analysis. A previous study reported that the Ga ion beam with a high accelerating voltage and a low current of below 1 nA can effectively reduce the uneven mechanical milling and thermal damage of the cathode layers [23]. Therefore, the accelerating voltage and Ga ion beam current were set to 30 kV and 0.8 nA, respectively, to minimize any unwanted damage. This condition was defined by the comparison test to determine the image quality equivalent to the ion beam damage-free image of the lamella sample prepared using ultramicrotoming. The field-of-view of the sectioned image included an area of 10 μm × 8 μm. The interval sectioning thickness produced by the FIB method was set to 15 nm, and the total number of sectioned images was 400. Wavelet-Fourier filtering was employed to remove image curtaining artifacts originating from the uneven vertical milling of the Ga ion beam across the sample. Digital processing was conducted for the stacking and alignment of the whole section images for each sample to obtain the reconstructed 3D data volumes of the PEM samples using a commercial 3D software package (Dragonfly ver. 2020.1, Object Research Systems Inc.). The reconstructed tomographic data were further processed for quantitative image segmentation analysis to measure the geometrical

parameters such as total porosity, pore size distribution, and pore-to-pore linkage. A pore network modeling software, i.e., the OpenPNM package written in Python [25], was used to visualize the three-dimensional network structure of the pores in each sample. In the data processing, the phase index determining the components for the network structure was set to 1 to equally utilize all binary images of the segmented pores. As a pre-filtering process for 3D modeling of pore structure, a Gaussian filter was used with a spherical structuring element of radius (R) of 4. The standard deviation (σ) of convolution kernel altering the smoothness of partitioned regions was set to 0.4. Then, the reconstructed pore network was visualized by artificial pores and throats inside the tomographic volumes of the porous cathode layer using the embedded code in the Dragonfly software. The initial large tomographic volumes were digitally divided into 16 small tomographic volumes of dimensions, 2 μm × 2 μm × 2 μm, to obtain the statistical data which illustrates the change of geometrical parameters before and after degradation cycling.

3. Results and discussion

3.1. Microstructural characterizations of PEM-FC before and after cycling

We have analyzed the overall cross-sectional structures of the cell to determine microstructural changes in the PEM-FC after cycling, and examined the Pt/Co-dispersed PEM electrodes in detail at high-magnification before and after 5,000 proton exchange cycles. Fig. 1(a and d) present the cross-sectional structures of

the PEM-FCs before and after the degradation cycling. It is observed that the thickness of the microporous anode layer is reduced by ∼20%. In comparison, that of the cathode layer is decreased slightly by ∼2% (Fig. 1g). The thicknesses of the anode and cathode layers before the cycling were 7.7 ± 0.7 and 9.9 ± 0.9 µm, respectively. After the degradation, those values were reduced to 6.2 ± 0.6 and 9.7 ± 1.1 µm, respectively. The cross-sectional PEM-FC samples were prepared using the freeze-fracture method to avoid structural distortion or damage during conventional cross-section sampling at room temperature [26]. This macroscale reduction of the electrode layer typically corresponds to the carbon support corrosion, which accompanies the aggregation of catalytic particles and their separation or isolation from the PEM electrolyte such as Nafion; this results in the reduction of the ECSA of the Pt-based catalyst [12–14,21,23,27]. Particularly, the layer contraction appears to be more noticeable in the anode layer, which can be attributed to the local hydrogen depletion-accelerated carbon corrosion caused by the non-uniform hydrogen transfer through the layer [28,29]. It is also observed that a dense and clean surface of the cathode was changed into a rough surface with several protruding particles (see the insets in Fig. 1a and d). SEM analysis of the cathode at a higher magnification (Fig. 1b and e) demonstrates that the overall microporous structure of the cathode seems to be well preserved after the degradation test. However, a more detailed inspection reveals that the original morphology of the carbon support that is filled with fine catalyst particles was changed to a lumpy and clotted structure. This results in the loss of an active surface area required for electrochemical reactions. Furthermore, the catalyst particles on the carbon support grew larger after the degradation cycling. Hereafter, the pristine and the degraded membrane cathodes are denoted as P-MC and D-MC, respectively.

We performed high-resolution ABF STEM imaging for the P- and D-MC samples to determine the degree of growth of the Pt/Co catalyst particles (Fig. 1c and f). In this imaging mode, heavy elements typically appear to be darker than the light elements due to the relatively strong scattering absorption effect on the ABF detector [30–32]. The statistical measurement of the ABF-STEM images of the two samples (Fig. 1h) clearly demonstrates that the mean size of the Pt/Co catalytic particles is increased by ∼20% and their size distribution also increases. The degree of the particle coarsening, including carbon corrosion, generally depends on the condition of proton exchange cycling [14]. In principle, this particle coarsening behavior is a thermodynamically spontaneous process which occurs during the electrochemical reaction at the electrode accompanying ion diffusion. This is known as Ostwald's ripening phenomenon, where the larger particles grow at the expense of the smaller ones due to the competitive balancing between the surface energy and bulk energy of the particles [33,34]. The microstructure observations indicate that the accelerated proton exchange cycling induced the carbon support corrosion and compaction, while concurrently reducing the ECSA of the Pt/Co catalysts owing to the agglomeration. Various studies have been conducted to present a detailed discussion on these structural degradations in terms of the FC performance lowering [11,13,21,35,36]. Similarly, we have observed a degradation in the *I-V* performance of the PEM-FCs at a high current density of 1.4 mA/cm^2 by ∼10% after 5000 potential cycles, as shown in Fig. 1(i). The degradation of the FC performance at such a high current density might be related to the decreased mass transport property, as well as the loss of ECSA [14], due to which a more detailed understanding for the structural change of the carbon support is essential. The elemental distribution maps of Pt, Co, F, and C included in the catalyst particles, ionomer, and carbon support, respectively, demonstrate that their spatial distribution conforms to the porous shape of the carbon support. However, the difference in the spatial distribution before and after the

degradation cycling remains unchanged apart from the coarsening of the Pt/Co particles (Fig. S1).

3.2. FIB-SEM tomography of PEM cathode layers

The information obtained by the 2D microscopy-based approach is limited to a localized region owing to its characteristics. Therefore, an extensive analysis performed on a much larger scale is required to obtain a better understanding of the degradation of the porous carbon support after cycling. Particularly, the variation in the surface morphology of the carbon support after the cycling must be determined along with the internal distribution of the pores and their hidden linkages within the carbon body in order to identify their physical links to the overall performance. An artificial volume reconstruction based on FIB-SEM tomography can be effectively utilized for such an analysis. We have employed the serial sectioning FIB-SEM tomography technique to analyze the 3D nature of the porous carbon support [17]. In the FIB-SEM instrument, the focused Ga ion beam is aligned to the sectioning plane of interest and is used to prepare a new section of the sample continuously, while the SEM is synchronized to automatically capture each sectioning plane of the sample (Fig. 2a). Subsequently, the FIB-SEM serial sectioning creates a stack of SEM images of a sample under observation. The contrast of the object in comparison to the empty space is enhanced in the image stack through digital processing which includes image alignment, filtering for noise and artifact, and binarized segmentation. Two major artifacts must be minimized in the construction of the entire image stack that is ready to be reconstructed in 3D: Ga ion beam-induced damage and artificially enhanced edge contrast of an object in the SEM imaging (Fig. S2). The instrumental setup for milling was optimized with a high accelerating voltage of 30 kV and a weak beam current of 0.8 nA to reduce the Ga ion beam-induced thermal damage [23]. However, uneven mechanical milling along the direction of the milling depth cannot be avoided; this phenomenon increases the surface roughness (curtaining effect) [37] and adversely affects the result of the segmentation process (Fig. S2a and c). We have addressed this issue by employing the vertical texture decomposition method based on wavelet-Fourier filtering [37,38] to the entire image stack and confirmed the removal of the vertical stripe contrast on each sectioning image (Fig. S2b and d). In SEM imaging, the secondary electron (SE) imaging mode is typically used to capture the surface morphology of a sample because it generates a strong contrast on the edge of an object due to a high yield of secondary electron emission. However, this image characteristic can decrease the reliability of object recognition and segmentation [39]. Conversely, the backscattered electron (BSE) imaging mode, in which the recoiled electrons are collected after the elastic interactions between the beam and the sample, demonstrates the dependence of atomic number in image contrast without the effect of the surface geometry of a sample. Therefore, the BSE imaging mode is virtually independent of the topographic contrast changes, which inevitably appear in the SE imaging mode (compare Fig. S2b and d). We have acquired a series of BSE images for the cathode layers in this imaging mode and performed a reliable object segmentation for the image stacks after noise filtering (rightmost, Fig. 2a). The newly obtained segmented image stack can be used to compose a 3D volume reconstruction.

Fig. 2(b and c) depict the resultant tomographic volumes of the PEM cathode layers before and after the degradation cycling, which is represented by dichotomizing the image contrast into porous carbon support (blue) and pores (yellow). The live rotation and perspective views of the two reconstructed cathode volumes and segmented pore structures for P- and D-MC samples, respectively, have been provided in supporting movies S1 and S2. It is difficult to identify any structural difference between the two tomographic
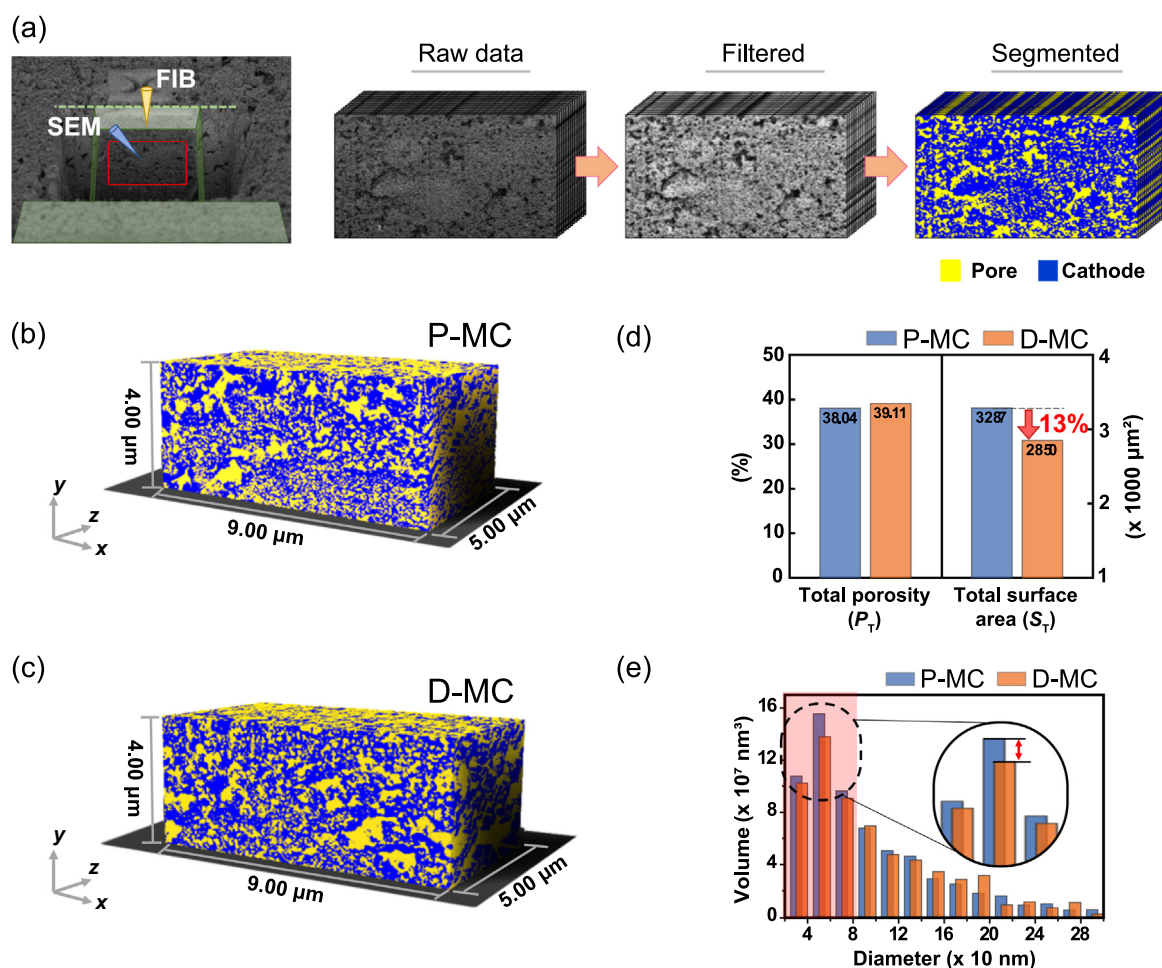
Fig. 2. FIB-SEM tomography of the cathode layers. (a) Typical workflow of FIB-SEM serial sectioning and digital processing to reconstruct a tomographic volume of the PEM cathode. (b and c) Perspective views of 3D reconstructed volumes of the P-MC and D-MC samples. The reconstructed dimension was set to 9 (x) μm × 4 (y) μm × 5 (z) μm. (d) Total porosities and surface areas of the PEM cathode samples. (e) Pore size distribution estimated from the two tomographic volumes.

volumes based on a visual analysis, which indicates that the pore content (i.e., total porosity) is similar before and after the cycling. Indeed, the total porosity (∼39%) of the D-MC measured after the cycling was observed to be similar to that (∼38%) of the P-MC (left graph, Fig. 2d). This result demonstrates that a simple 3D visualization and the measurement of the pore content (total porosity, P_T) cannot be considered as a deterministic parameter in the estimation of the structural degradation that occurs during cycling. Several previous results have consistently demonstrated a similar trend to our measurements, which indicates that the FIB-SEM tomography has not been applied often for the evaluation of the structural deterioration after cycling, apart from the survey of the pristine structural characteristics based on the synthesis condition. A signature for the reduction of small pores (less than ∼100 nm in size) in the D-MC is observed in the comparison of pore size distributions of the P- and D-MC samples (Fig. 2e) but is very subtle. Conversely, the total surface area (S_T) of the carbon support was observed to be reduced by ∼13% after the cycling (right graph, Fig. 2d). The reduction of the S_T is attributed to the collapse or compaction of the porous carbon structure due to the oxidation of the carbon support during the electrochemical cycling. The resultant loss of the ECSA is a crucial factor in promoting the catalyst agglomeration, which results in the performance degradation. Therefore, the magnitude of the S_T reduction can be considered as an indicator to determine the structural degradation of the electrode when compared to the pristine state. As the S_T varies,

while the P_T is similar to each other, we infer that small pores and surface morphology are considerably altered within the porous PEM layer, indicating that they have a more significant effect on the electrochemical performance of the electrode. Therefore, a detailed analysis of the change in the surface structure, local pore distribution, and their networking in 3D is crucial for a better understanding of the structural degradation behavior.

3.3. Local segmentation analysis on tomographic pore volumes

We have digitally extracted the pore volumes of the two samples from the overall tomographic volumes and segmented them into 16 local pore volumes (2 μm × 2 μm × 2 μm) as subsets for statistical analysis on the related structural parameters to determine the change in the local structure between the P-MC and D-MC (Fig. 3a and b). Based on this post-processing, we can present a more reliable evaluation of the variation of the geometrical parameters of the local surface area (S_L) and local porosity (P_L) with statistical significance after cycling, and present a correlation between the change of S_L when compared to that of P_L. Fig. 3(c) presents the distribution of the S_L corresponding to the P_L for the two samples. It can be observed that the D-MC (orange square) presents a much narrower distribution of S_L, whereas the distribution of P_L is comparable to that of the P-MC (blue triangle). The average porosity (P_L) for the two samples was similarly estimated to be 37.8% ± 3.6% and 38.9% ± 3.4%, respectively, based on this
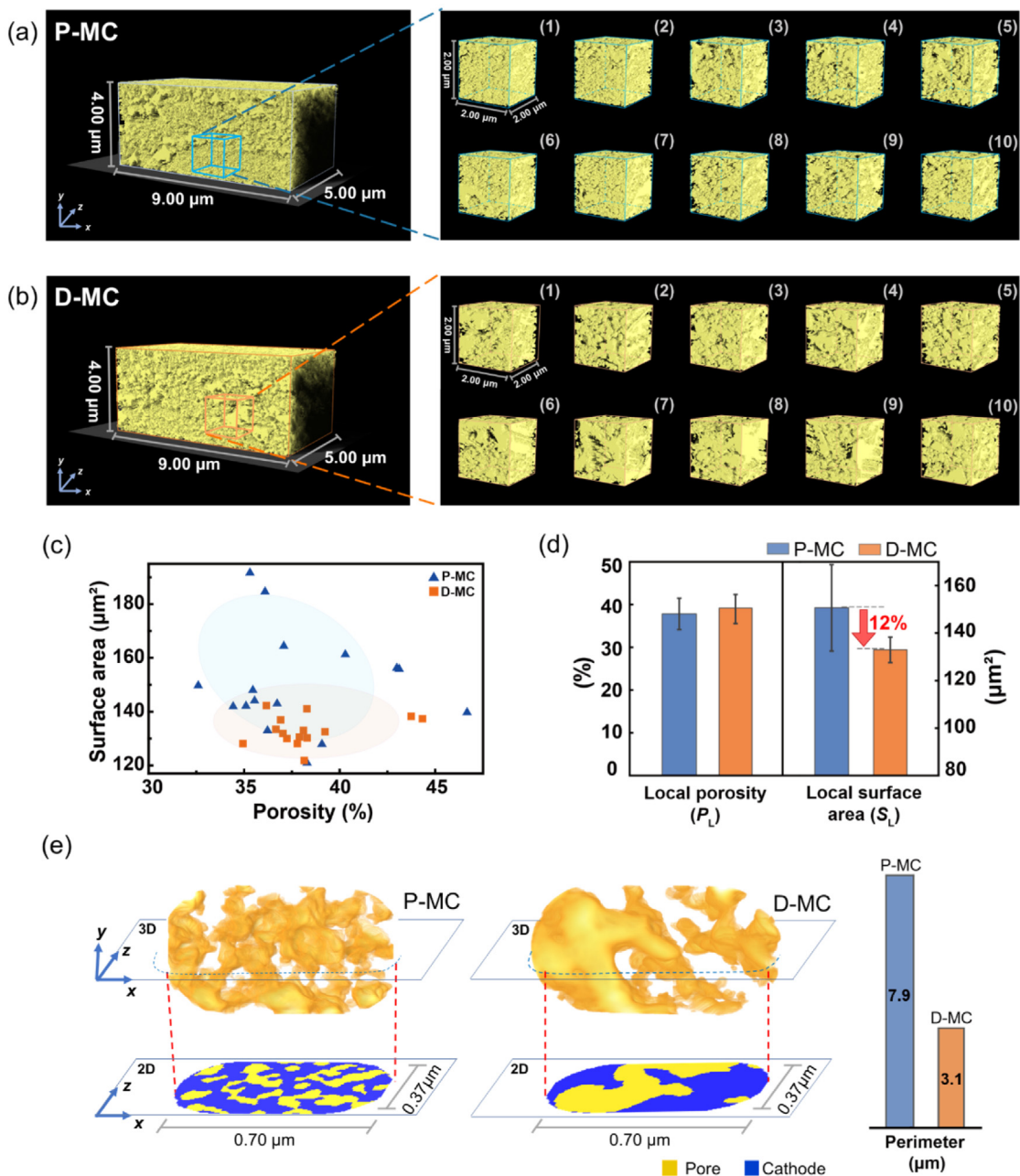
Fig. 3. Segmentation analysis of the reconstructed cathode layers. (a and b) Extracted 3D pore structures from the reconstructed P-MC and D-MC samples. Example array of segmented local pore volumes of the two samples for statistical pore structure analysis, which were disjoined from the parent 3D pore volumes by a constant square block with dimension of 2 (x) μm × 2 (y) μm × 2 (z) μm. (c) Distribution plot of surface area and porosity measured from 16 segmented local volumes for the P-MC (blue) and D-MC (orange) samples, respectively. (d) Column graphs presenting the average values of local porosities and surface areas with the statistical deviation. (e) Representative 3D local structures of the two samples: (left) the P-MC and (right) the D-MC, respectively. The projected MEA structures are correspondingly displayed below each 3D volumes, which were cut by the x-z plane. The total perimeters of the two samples measured from the dissected images are plotted on the right.

segmentation analysis. However, the average surface area (S_L) and its scatter (Δ) present a significant discrepancy between the P- and D-MC samples (Fig. 3d): 150.2 ± 18.2 and 132.5 ± 5.4 μm², respectively. The S_L is reduced by ~12% after cycling, which is comparable to the change in the total surface area, S_T. Particularly, the large scatter of the measured surface areas for the P-MC reduces to a small range for the D-MC (Fig. 3c). This result indicates that the structural degradation of the carbon support typically leads to the compaction or collapse of small pores near the surface. Essentially, a wide branched surface of the carbon support is decreased to a narrow, smooth surface, rendering the exposed active surface

area reduced by the corrosion reaction: C + 2H₂O → CO₂ + 4H⁺ + 4e⁻. The catalysts can be physically detached from the PEM/carbon support after this negative reaction. A chain of the structural disintegration consequently degrades the mass transport in the catalyst layer.

Our study directly supports the previous studies which state that a substantial loss of the electrochemical performance can be attributed from a severe carbon corrosion which occurs during a lifetime of the PEM-FC. Based on this perspective, we have emphasized the local structural inspection on the porous surface morphology when compared to the total pore fraction while

evaluating the degree of degradation using electron tomography. Fig. 3(e) depicts small internal pore volumes extracted from the segmented volumes (denoted by no. 1) of the P- and D-MC to visually demonstrate the change in the fine porous surface after cycling. We have observed that several fine pores near the carbon surface are coalesced into a large pore as the degradation cycles proceeds, resulting in a loss of exposed surface area to the reactant gases. The *x-z* cross-sections for the two local volumes demonstrate a clear difference in the surface morphology (see bottom figures in Fig. 3e). For example, the circumference of the carbon support for the same sectioning area of the P- and D-MC volumes was measured to be 7.9 and 3.1 μm, respectively, even though the fractional area (0.38) of the pores for the P-MC is smaller than that (0.46) measured for the D-MC. This comparison demonstrates that the change in the local surface morphology is one of the crucial factors which affects the structural degradation.

3.4. Distribution of pores and their networking in tomographic volumes

The catalyst particles entrapped within closed pores or detached from carbon support cannot interact with the ionomer offering ion conduction pathway. The fewer the number of pores that are interconnected with each other, the greater the number of catalyst particles that are isolated from the conduction pathway, thus impeding oxygen reduction reaction kinetics [1,40]. Therefore, determining the 3D distribution of the pores and their connectivity within the carbon structure is important to understand the cycling-induced structural degradation. We have analyzed the pore geometry and the 3D network structure of the pores inside the porous carbon support based on a pore network analysis to address this issue [25]. In this approach, the pore spaces are considered as a network of pipes in order to measure the linear length of the conduit from pore to pore in the tomographic volumes of porous materials.

Fig. 4 presents the results for the two segmented volumes of P- and D-MC. The top and bottom figures in Fig. 4(a) illustrate the 3D distribution of the pores within the P- and D-MC samples, respectively. In this data processing approach, the location of the pores and their size were artificially assigned by the selection of the largest sphere filling for the inside of the irregular shape of a real pore. We have counted the total number of pores for the two samples, and observed that they are similar, i.e., 1109 and 1095 for P- and D-MCs, respectively (Fig. 4c). We expect that the distribution of the pore sizes in the P-MC would be broader for a small pore range than in the D-MC based on similar P_L values for the segmented volumes of the two samples unlike the S_L values (Fig. 3d). Indeed, we notice from a comparison of the histograms of the pore sizes for the two samples (top and middle, Fig. 4d), that small pores are richer in the P-MC than in the D-MC. There are ~8% more small pores (less than 100 nm) in the P-MC than in the D-MC. From the difference plot between the histograms of D-MC and P-MC (bottom, Fig. 4d), it is clearly visible how the size range of the pores changed after the degradation cycling. We see that the small pores less than 100 nm in size were considerably reduced, while the larger pores between 100 and 200 nm in size, were rather increased after the cycling. Meanwhile, no noticeable change in the larger pores more than 200 nm was observed. This structural characteristic explains the reason for the significant reduction of the S_L in the D-MC sample, as shown in Fig. 3. As a signature of the carbon corrosion, we have observed that the collapse of carbon support results in the reduction of small pores less than 100 nm in size near the surface.

For the assigned pore, which is connected to the adjacent pores with space channels (assumed to be linear) in the tomographic volume, the number of the connected pores, i.e., the pore-to-pore linkage, can be digitally counted. The number of connected neighboring pores for each pore is represented by the false color scale presented at the bottom of Fig. 4(a). The result for the P-MC sample demonstrates that the connectivity between adjacent pores is high. In contrast, the networking of the neighboring pores appears to be reduced for the D-MC sample. For the pores larger than 10 nm, the average number of connected pores was reduced from 4.6 to 4.1 after 5000 degradation cycles. Consequently, it is
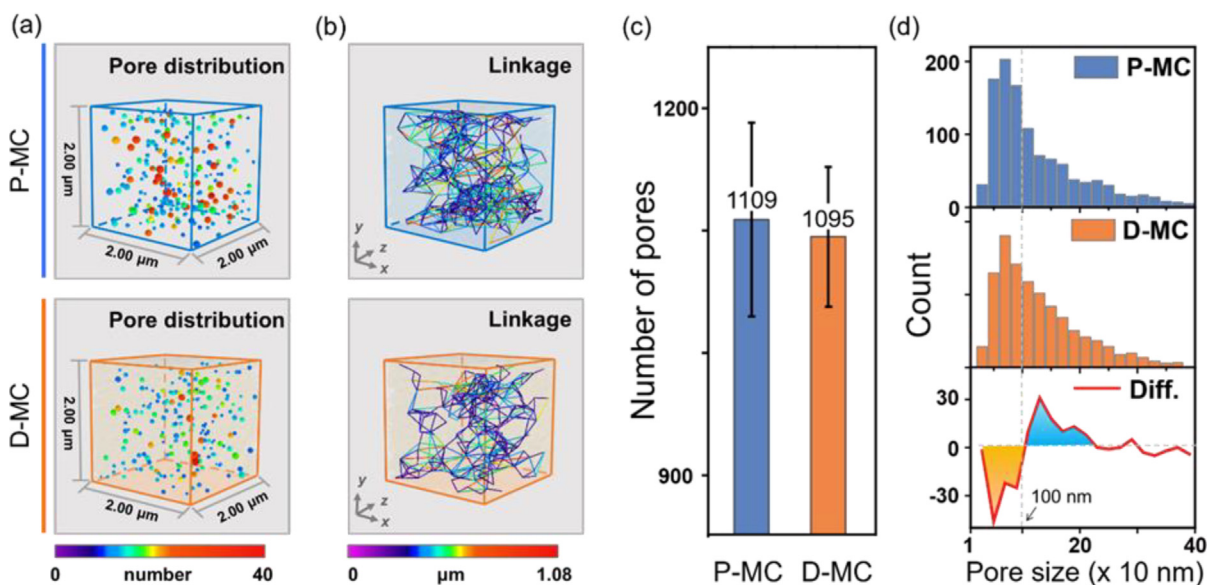

Fig. 4. Pore distribution network analysis for the P- and D-MC samples. (a) 3D distribution of pore sizes classified corresponding to the number of connected neighboring pores. The pores connected to fewer than five adjacent pores were omitted for clear visualization. Note that the number of pores connected to a pore centroid is represented by the false color scale presented at the bottom and the size of each ball indicates the measured pore size, assuming that the pore size is defined by the largest diameter of the sphere filling for the inside of the irregular shape of the pore. (b) 3D distribution of linear linkages between the neighboring pore centroids. Note that the different linkage lengths between the pore centroids are false-colored corresponding to the bottom color scale for visualization. (c) Column graphs showing total number of pores. (d) Histograms showing pore size distribution for the P-MC (top, blue) and D-MC (middle, orange) samples. Bottom graph depicts the difference plot between the histograms of D-MC and P-MC, showing the ranges of pore size which were changed after the degradation cycling.

estimated that the connectivity between the pores is reduced by ~10%. The pore connectivity for the P-MC and D-MC samples can be alternatively represented by depicting the linkage depth of the network between the adjacent pores (Fig. 4b). The result presents a clear 3D representation of pore channels in the P- and D-MC layers. The pore channel volumes are represented at 20% of the raw data size to better visualize the network of linear channels. It can be clearly observed that the dense pore channels in the P-MC are significantly reduced in the D-MC. The average length of the pore channels for the pores connected to more than seven neighboring pores was observed to be reduced from 360 (P-MC) to 330 nm (D-MC). Furthermore, the number of the pores connected to more than seven neighboring pores decreased from 780 (P-MC) to 472 (D-MC), which is a reduction of approximately 38%. This analysis demonstrates that the reduction of pore linkage must be considered an important structural aspect of the carbon support degradation, which contributes to the lowering of the gas permeability during fuel cell operation.

Our segmented tomography analysis presents four structural features of the D-MC when compared to the P-MC, which are as follows. Firstly, the average surface area of carbon support was significantly reduced by ~12%, whereas the change of porosity was insignificant. Secondly, the change in the surface area was largely based on the location, emphasizing the importance of statistical interpretation. Thirdly, the small pores (less than 100 nm in size) were noticeably reduced by ~8% due to the collapse of the carbon support. Lastly, the 3D linkage of pores was reduced by ~10%. Based on this extensive tomographic analysis, we have observed that the structural parameters such as surface area, local pore distribution, and their 3D networking must be considered in the estimation of carbon support degradation.

4. Conclusions

We have employed advanced segmentation analysis of FIB-SEM-based tomographic PEM volumes to effectively visualize, elucidate, and quantitatively evaluate the structural degradation of the porous carbon support in 3D at the nanoscale through the statistical interpretation of geometrical parameters. Although there was no significant difference in the overall porosity before and after the cycling, the surface area, pore size distribution, and their connectivity in 3D are significantly varied due to the degradation phenomenon. This result indicated that the changes in these parameters describing the carbon support morphology are closely correlated to the degradation of the PEM performance. Therefore, they are used as barometers to evaluate the degree of carbon-corrosion-mediated PEM degradation. The three-dimensionally resolved collapse (or compaction) of the carbon support was highlighted as one of the structural origins of the degradation and is expected to hinder the electrochemical accessibility of catalyst particles to oxygen through the porous layer. Our advanced tomographic approach presented a deeper understanding of the structural degradation phenomenon of carbon supports during the FC operation and can be implemented for the design of the cathode layer for durable PEM FCs as the structural changes were parameterized by the post-digital processing.

Declaration of competing interest

The authors declare that they have no known competing financial interests or personal relationships that could have appeared to influence the work reported in this paper.

Acknowledgments

Appendix A. Supplementary data

Supplementary data to this article can be found online at https://doi.org/10.1016/j.jechem.2022.07.036.

References

[1] D.A. Cullen, K.C. Neyerlin, R.K. Ahluwalia, R. Mukundan, K.L. More, R.L. Borup, A.Z. Weber, D.J. Myers, A. Kusoglu, Nature Energy 6 (2021) 462–474.
[2] I. Staffell, D. Scamman, A. Velazquez Abad, P. Balcombe, P.E. Dodds, P. Ekins, N. Shah, K.R. Ward, Energy Environ. Sci. 12 (2019) 463–491.
[3] W.S. Jung, J. Energy Chem. 27 (2018) 326–334.
[4] M. Kiani, J. Zhang, Y. Luo, C. Jiang, J. Fan, G. Wang, J. Chen, R. Wang, J. Energy Chem. 27 (2018) 1124–1139.
[5] K.-D. Kreuer, S.J. Paddison, E. Spohr, M. Schuster, Chem. Rev. 104 (2004) 4637–4678.
[6] A. Kraytsberg, Y. Ein-Eli, Energy Fuels 28 (2014) 7303–7330.
[7] M.M. Tellez-Cruz, J. Escorihuela, O. Solorza-Feria, V. Compañ, Polymers 13 (2021) 3064.
[8] S.J.C. Cleghorn, X. Ren, T.E. Springer, M.S. Wilson, C. Zawodzinski, T.A. Zawodzinski, S. Gottesfeld, Int. J. Hydrogen Energy 22 (1997) 1137–1144.
[9] H. Zhang, P.K. Shen, Chem. Rev. 112 (2012) 2780–2832.
[10] C. Wang, M. Ricketts, A.P. Soleymani, J. Jankovic, J. Waldecker, J. Chen, J. Electrochem. Soc. 168 (2021) 044507.
[11] L. Castanheira, W.O. Silva, F.H.B. Lima, A. Crisci, L. Dubau, F. Maillard, ACS Catal. 5 (2015) 2184–2194.
[12] J.C. Meier, C. Galeano, I. Katsounaros, A.A. Topalov, A. Kostka, F. Schüth, K.J.J. Mayrhofer, ACS Catal. 2 (2012) 832–843.
[13] Y.-J. Wang, D.P. Wilkinson, J. Zhang, Chem. Rev. 111 (2011) 7625–7651.
[14] H. Schulenburg, B. Schwanitz, N. Linse, G.G. Scherer, A. Wokaun, J. Krbanjevic, R. Grothausmann, I. Manke, J. Phys. Chem. C 115 (2011) 14236–14243.
[15] Y. Zheng, T. Deng, W. Zhang, W. Zheng, J. Energy Chem. 47 (2020) 210–216.
[16] W. Zhang, L.T. Kuhn, P.S. Jørgensen, K. Thydén, J.J. Bentzen, E. Abdellahi, B.R. Sudireddy, M. Chen, J.R. Bowen, Microsc. Microanal. 19 (2013) 501–505.
[17] M.D. Uchic, L. Holzer, B.J. Inkson, E.L. Principe, P. Munroe, MRS Bull. 32 (2007) 408–416.
[18] T.L. Burnett, R. Kelley, B. Winiarski, L. Contreras, M. Daly, A. Gholinia, M.G. Burke, P.J. Withers, Ultramicroscopy 161 (2016) 119–129.
[19] J.-H. Shim, Y.-H. Kim, H.-S. Yoon, H.-A. Kim, J.-S. Kim, J. Kim, N.-H. Cho, Y.-M. Kim, S. Lee, ACS Appl. Mater. Interfaces 11 (2019) 4017–4027.
[20] J.D. Arregui-Mena, P.D. Edmondson, A.A. Campbell, Y. Katoh, J. Nucl. Mater. 511 (2018) 164–173.
[21] F. Hegge, J. Sharman, R. Moroni, S. Thiele, R. Zengerle, M. Breitwieser, S. Vierrath, J. Electrochem. Soc. 166 (2019) F956–F962.
[22] N. Ramaswamy, S. Kumaraguru, W. Gu, R.S. Kukreja, K. Yu, D. Groom, P. Ferreira, J. Electrochem. Soc. 168 (2021) 024519.
[23] M. Okumura, Z. Noda, J. Matsuda, Y. Tachikawa, M. Nishihara, S.M. Lyth, A. Hayashi, K. Sasaki, J. Electrochem. Soc. 164 (2017) F928–F934.
[24] S.W. Lee, S.R. Choi, J. Jang, G.-G. Park, S.H. Yu, J.-Y. Park, J. Mater. Chem. A 7 (2019) 25056–25065.
[25] J. Gostick, M. Aghighi, J. Hinebaugh, T. Tranter, M.A. Hoeh, H. Day, B. Spellacy, M.H. Sharqawy, A. Bazylak, A. Burns, W. Lehnert, A. Putz, Comput. Sci. Eng. 18 (2016) 60–74.
[26] N.J. Severs, Nature Protocols 2 (2007) 547–576.
[27] E.A. Wargo, T. Kotaka, Y. Tabuchi, E.C. Kumbur, J. Power Sources 241 (2013) 608–618.
[28] X.G. Yang, Q. Ye, P. Cheng, Int. J. Heat Mass Transf. 55 (2012) 4754–4765.
[29] P.T. Yu, W. Gu, J. Zhang, R. Makharia, F.T. Wagner, H.A. Gasteiger, in: Polymer Electrolyte Fuel Cell Durability, Springer, New York, 2009, pp. 29–53.
[30] Y.-M. Kim, S.J. Pennycook, A.Y. Borisevich, Ultramicroscopy 181 (2017) 1–7.
[31] O. Kwon, Y.I. Kim, K. Kim, J.C. Kim, J.H. Lee, S.S. Park, J.W. Han, Y.-M. Kim, G. Kim, H.Y. Jeong, Nano Lett. 20 (2020) 8353–8359.
[32] W.-S. Jang, Y. Jin, Y.-H. Kim, S.-H. Yang, S.J. Kim, J.A. Hong, J. Baik, J. Lee, H. Lee, Y.-M. Kim, Appl. Catal. B: Environ. 305 (2022) 121083.
[33] S.Y. Chung, Y.M. Kim, J.G. Kim, Y.J. Kim, Nat. Phys. 5 (2009) 68–73.
[34] C.J. Gommes, Nanoscale 11 (2019) 7386–7393.

[35] F.A. de Bruijn, V.A.T. Dam, G.J.M. Janssen, Fuel Cells 8 (2008) 3–22.
[36] J. Wu, X.Z. Yuan, J.J. Martin, H. Wang, J. Zhang, J. Shen, S. Wu, W. Merida, J. Power Sources 184 (2008) 104–119.
[37] J. Schwartz, Y. Jiang, Y. Wang, A. Aiello, P. Bhattacharya, H. Yuan, Z. Mi, N. Bassim, R. Hovden, Microsc. Microanal. 25 (2019) 705–710.

[38] D. Kim, S. Lee, W. Hong, H. Lee, S. Jeon, S. Han, J. Nam, Microsc. Microanal. 25 (2019) 1139–1154.
[39] M. Cantoni, L. Holzer, MRS Bull. 39 (2014) 354–360.
[40] A. Kusoglu, D. Kushner, D.K. Paul, K. Karan, M.A. Hickner, A.Z. Weber, Adv. Funct. Mater. 24 (2014) 4763–4774.